Journal of Materials Chemistry A

ROYAL SOCIETY OF CHEMISTRY

PAPER

Cite this: *J. Mater. Chem. A*, 2021, **9**, 1795

A highly stretchable strain sensor with both an ultralow detection limit and an ultrawide sensing range†

Hua Li,[ab] Jianwen Chen,[ac] Xiaohua Chang,[a] Youquan Xu,[a] Guiyan Zhao,[b] Yutian Zhu *[a] and Yongjin Li *[a]

Received 11th November 2020
Accepted 10th December 2020

DOI: 10.1039/d0ta10990h

rsc.li/materials-a

Stretchable strain sensors have promising applications in many fields, including soft robotic skin, health monitoring, wearable electronics, and so on. Among the various properties of stretchable strain sensors, the low detection limit and wide sensing range are the two most critical properties that determine their practical application in the above fields. However, it is still a great challenge to achieve both an ultralow detection limit and ultrawide sensing range at the same time, and there often needs to be a tradeoff between them. Herein, we propose a simple route to design a stretchable strain sensor with both an ultralow detection limit and an ultrawide sensing range by the combination of the electrospinning technique and ultrasonication anchoring technique. Specifically, thermoplastic polyurethane (TPU) is fabricated into a highly stretchable porous film and carbon nanotubes (CNTs) are anchored onto the surface of TPU nanofibers assisted by ultrasonication, and then assembled with two Cu electrodes to fabricate the strain sensor. Attributed to the multiscale evolution of the conductive network under stretching, the designed strain sensor exhibits many outstanding merits, such as an ultra-low detection limit (0.05%), an ultrawide sensing range from 0.05% to 600%, a fast response time of 75 ms, and excellent durability. Because of these outstanding merits, the TPU@CNT strain sensor can detect both the subtle strain change caused by the sound of a piano and the large strain change caused by the large-scale motions of joints. Moreover, it is found that TPU@CNT sensor responds to temperature and humidity, which has great potential in temperature sensors and humidity sensors.

1. Introduction

In the past ten years, there has been an increasing demand for stretchable and wearable strain sensors because of their important applications in human motion detection, healthcare monitoring, soft robotics, and so on.[1] Basically, stretchable strain sensors usually transduce mechanical deformations induced by external forces into electrical signals, thus sensing the external force by these signals.[2] Based on this principle, various conductive components, including intrinsically conductive polymers, carbon black, carbon nanotubes, graphene, silver nanowires and liquid metal, are combined with stretchable polymeric substrates to create versatile stretchable strain sensors.[3–28]

To serve as stretchable strain sensors for various applications, an ultralow detection limit and wide sensing range are two key and essential requirements. An ultralow detection limit endows the sensors with the capacity to detect subtle strain changes caused by pulsation, such as pulse wave peaks, percussion waves, tidal waves, and diastolic waves, which is undoubtedly important for disease diagnosis and real-time health monitoring. On the other hand, it also needs a wide sensing range (>100%) for the sensor to detect large-scale motions such as joint movements simultaneously. To achieve the high strain sensitivity, a brittle thin film of conductive nanoparticles deposited on top of a stretchable layer is widely utilized as the sensing layer to develop microcrack-assisted resistive strain sensors.[29–31] For instance, Kang *et al.*[32] designed a sensor with ultrahigh sensitivity based on nanoscale cracks of a platinum film on an elastomer polymer. However, the maximum working strain of this sensor is only 2% because the metal film will be destroyed irreversibly beyond the maximum strain. The maximum working strain can be extended to *ca.* 20–80% by using conductive nanoparticles with a large ratio of length to diameter to generate the conductive layer of the microcrack-assisted resistive strain sensor. For example, Singh *et al.*[33] used pristine and doped graphene as the

[a]*College of Materials, Chemistry and Chemical Engineering, Hangzhou Normal University, No. 2318 Yuhangtang Rd., Cangqian, Yuhang District, Hangzhou, 311121, China. E-mail: ytzhu@hznu.edu.cn; yongjin-li@hznu.edu.cn*

[b]*College of Petrochemical Engineering, Liaoning Shihua University, No. 1 West Section of Dandong Rd., Wanghua District, Fushun, Liaoning Province, 113001, China*

[c]*State Key Laboratory of Polymer Physics and Chemistry, Changchun Institute of Applied Chemistry, Chinese Academy of Sciences, Changchun 130022, China*

† Electronic supplementary information (ESI) available. See DOI: 10.1039/d0ta10990h

sensing layer to develop an ultrasensitive strain sensor due to crack generation and overlapping scale separation in both doped and intrinsic graphene, which exhibited a very small detection limit (0.01%). However, its working strain range was limited to 26%. Liao *et al.*[34] demonstrated a microcrack-assisted strain sensor by deposing silver nanowires on top of polydimethylsiloxane. The resulting sensor exhibited ultrahigh sensitivity and a relatively wide strain sensing range (<60%). Through designing the complex conductive network microstructures, only very few studies[35–37] have extended the upper limit of the working strain to >100%. Sun *et al.*[38] constructed a micropatterned double-layer Au/SWCNT composite structure to design an ultrasensitive and stretchable strain sensor, which exhibited both a wide detection range (up to 100% strain) and a low limit of detection (0.1% strain). Currently, it is still a great challenge to fabricate stretchable sensors with both an ultralow detection limit and an ultrawide sensing range.

Herein, we demonstrate a simple strategy to fabricate a highly stretchable strain sensor with both an ultralow detection limit and an ultrawide sensing range by the combination of the electrospinning technique and ultrasonication anchoring technique. Specifically, a highly stretchable thermoplastic polyurethane (TPU) fibrous mat is fabricated using the electrospinning technique at first, and then CNTs are decorated onto the surface of TPU nanofibers by the ultrasonication anchoring technique to fabricate the stretchable sensors. Attributed to the multiscale evolution of the conductive network, the resulting sensor exhibits many superior merits, including an ultralow detection limit (<0.05%), an ultrawide strain sensing range (up to 600%), excellent linearity to strain in the strain range from 0.05% to 600%, and good stability and repeatability in the sensing performance. These fascinating merits allow the strain sensor to precisely detect both the subtle strain change caused by the sound of a piano and the large strain change caused by the large-scale motions of joints.

2. Experimental

2.1 Materials

Thermoplastic polyurethane (TPU, Elastollan 1185A), known for its excellent elasticity as a typical elastomer, was chosen for electrospinning and was obtained from BASF Co., Ltd. Both *N*,*N*-dimethylformamide (DMF, Z99.5%, analytical reagent) and tetrahydrofuran (THF, Z90%, analytical reagent) were provided by Sinopharm Chemical Reagent Co., Ltd, China. Deionized water was obtained from Sichuan ULUPURE Technology Co., Ltd, China. The highly conductive carbontube slurry (CNTs, diameter: 7–11 nm; 4 wt%) was obtained from ENN Graphene Technology Co., Ltd.

2.2 Preparation of the TPU fibrous mat by electrospinning

The TPU fibrous mat was fabricated through the electrospinning technique. First, 5.0 g TPU granules were dissolved in a DMF/THF mixed solution with a certain ratio of 25 wt% (the volume ratio of DMF/THF is 1 : 1). The mixture was mechanically stirred for 3.5 h to obtain a homogeneous spinning solution. Second, a syringe with a spinneret was filled with the resulting TPU solution for electrospinning. Typical electrospinning experiments were performed at 15 kV, with a polymer solution feed rate of 0.1 mL h^{-1}. Aluminum foil was selected as a static and grounded collector, and its distance to the needle tip was 15 cm.

2.3 Preparation of the TPU@CNT strain sensor

A CNT slurry was dispersed in deionized water. CNT dispersions were subjected to ultrasonication for 0.5 h in an ice water bath on a SCIENTZ-IID Ultrasonic Homogenizer (Ningbo Scientz Biotechnology Co., Ltd, China). The TPU fibrous mat membranes were ultrasonically treated in the CNT dispersions for 1 h in an ice water bath with a nominal frequency of 20 kHz and a power of 250 W. Then, the TPU@CNT fibrous membranes were washed thoroughly with deionized water several times to remove the unanchored CNTs. Finally, two Cu electrodes were loaded onto a 3 cm × 0.5 cm TPU@CNT fibrous membrane to assemble the stretchable strain sensor (the distance between the two copper electrodes is 2 cm, and the thickness of the TPU@CNT fiber membrane is *ca.* 0.2–0.3 mm).

2.4 Characterization

The stretching electromechanical behaviors of TPU@CNT strain sensors were analyzed on an electronic universal tensile testing machine (INSTRON5966, USA) coupled with a digit precision multimeter (KEITHLEY, DMM 7510, USA). The temperature sensing behaviors of TPU@CNT sensors were analyzed on an INSTEC coupled with a KEITHLEY. The resistance of the TPU@CNT sensor was recorded during heating from 30 °C to 40 °C at a heating rate of 5 °C min^{-1}, followed by natural cooling from 40 °C to 30 °C. The humidity sensing performances of TPU@CNT sensors were analyzed in a temperature and humidity chamber (PCTHI-150T, Shanghai STIK Co., Ltd., China) coupled with a KEITHLEY. The humidity was increased from 50% RH to 95% RH at first, and then was decreased from 95% RH to 50% RH at a constant temperature of 20 °C. During this process, the resistance of the sensor was recorded online. The surface morphologies of the TPU@CNT strain sensors were analyzed by scanning electron microscopy (SEM, HITACHI S-4800).

3. Results and discussion

To better understand the fabrication process of stretchable TPU@CNT sensors, we present a schematic diagram in Fig. 1 to illustrate this process. First, the TPU fibrous membrane is fabricated using the electrospinning technique. Second, the TPU fibrous membrane then serves as a stretchable substrate for decoration with CNTs *via* the ultrasonication anchoring technique, which leads to a percolated conductive network on the surface of TPU fibers. Finally, the TPU@CNT membrane is assembled with two electrodes to design the stretchable strain sensor.

The morphologies of the TPU fibrous membrane before and after decorating with CNTs are visualized by SEM (Fig. 2). It is

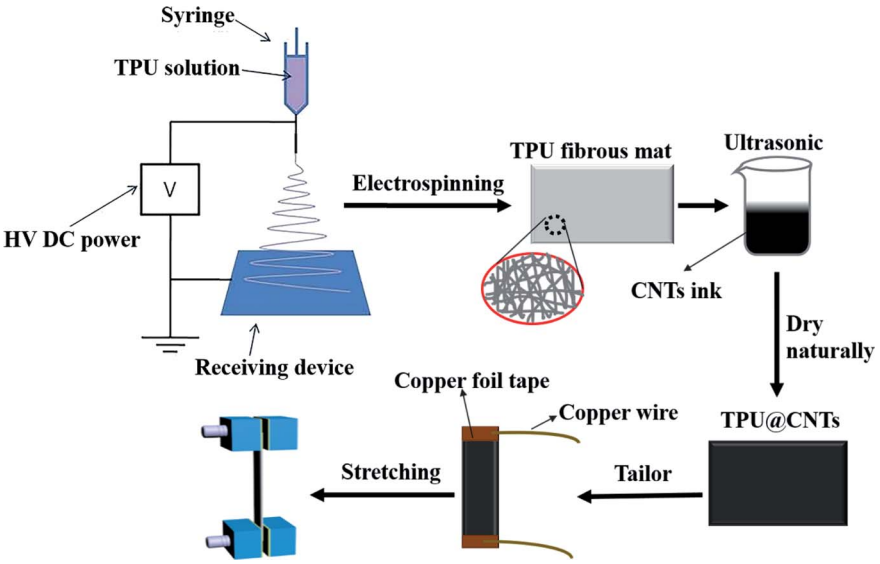

Fig. 1 Schematic illustration for the fabrication of the stretchable TPU@CNT strain sensor.

observed that TPU fibers possess a smooth surface before ultrasonication treatment (Fig. 2a–c). Clearly, after 60 min of ultrasonication treatment in an ice water bath, TPU fibers are covered by a thin layer of CNTs, which form excellent conductive pathways on the continuous fiber surfaces (Fig. 2a′–c′). Fig. 2b′ and c′ show that most CNTs are entangled together on the surface of TPU fibers. More interesting, it is observed that CNTs are anchored onto the TPU fibers at the fractured surface of the TPU fibers (Fig. 2c′). This ensures the stability of the CNT sensing layer during cyclic stretching and release.

The sensing performance of the designed TPU@CNT strain sensor is analyzed using the combination of an electronic universal tensile testing machine and a digit precision multimeter. The sensor is subjected to various cyclic stretching–release processes while its resistance changes are recorded simultaneously. As can be seen in Fig. 3a, the TPU@CNT strain sensor exhibits stable and repeatable sensing behavior during the cyclic stretching–release measurements at a strain as low as 0.05%. To the best of our knowledge, this detection limit of the strain is ultralow compared to those in previous work.[38–41] More

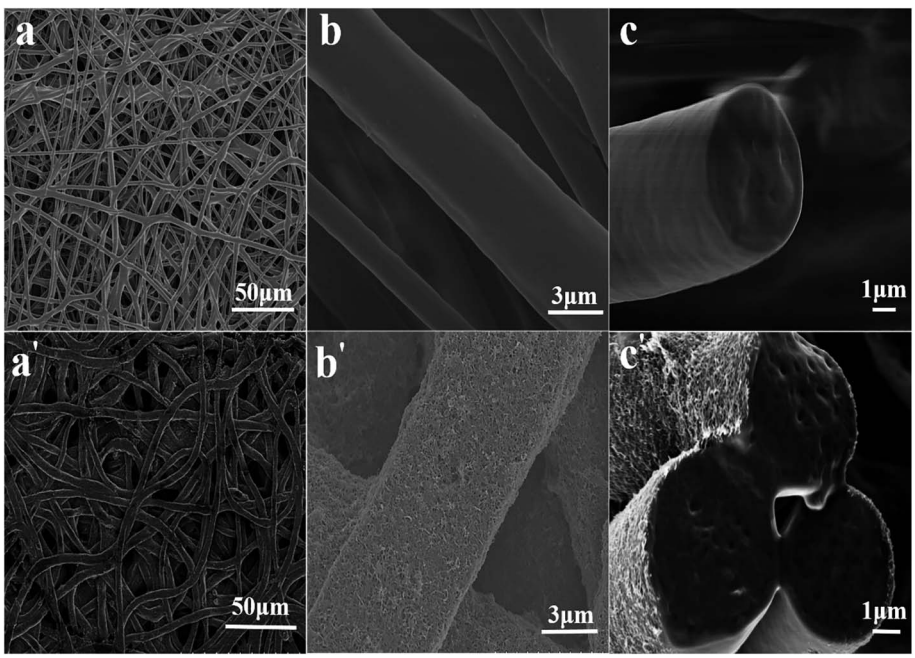

Fig. 2 Images (a–c) showing the SEM images of the pure TPU fibrous membrane at different magnifications; the (a′–c′) corresponding SEM images of the CNT decorated TPU fibrous membrane after 60 min of ultrasonication treatment in an ice water bath at different magnifications.

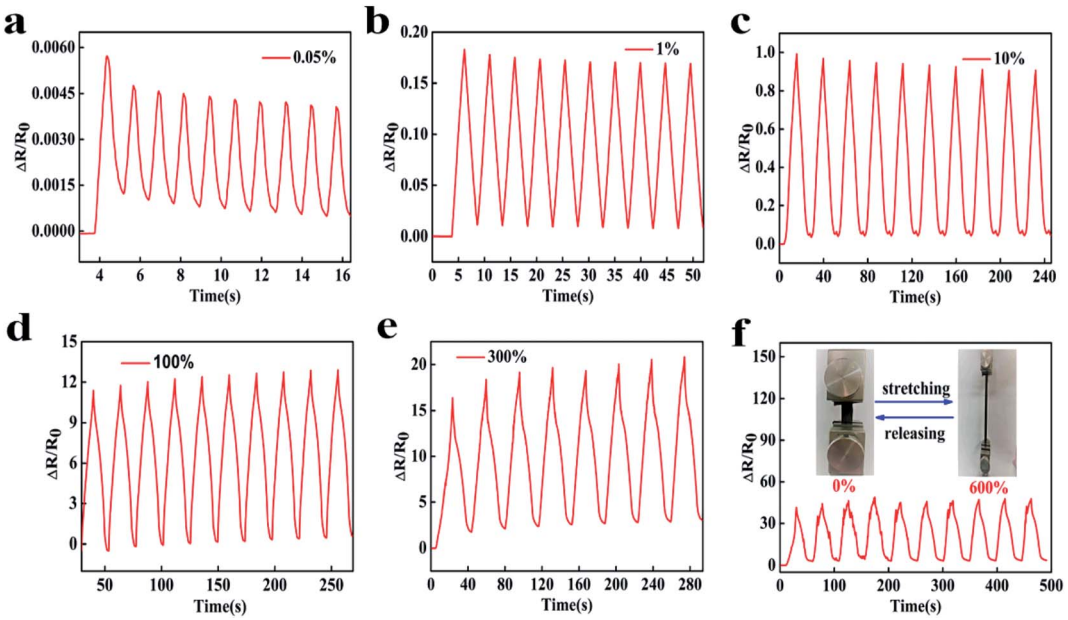

Fig. 3 Dynamic response behaviors of the TPU@CNT strain sensor during stretching–release cycles at various strains of (a) 0.05%, (b) 1%, (c) 10%, (d) 100%, (e) 300% and (f) 600%.

importantly, it is observed that the TPU@CNT strain sensor also displays excellent sensing performance at strains of 1%, 10%, 100%, 300%, and 600% (Fig. 3b–f). This implies that the TPU@CNT strain sensor can fully cover an ultra-wide strain sensing range from 0.05% to 600%, which can well solve the problem of stretchable strain sensors being unable to have both an ultralow detection limit and ultrawide sensing range.

Stepwise cyclic stretching–release tests are performed to evaluate the discrimination and stability of the TPU@CNT strain sensor, as shown in Fig. 4a and b. The strain sensor retains its excellent sensing characteristics either under a small stepwise increase of the strain from 0.05% to 0.5% at a rate of 0.05% or under a relatively large stepwise increase of the strain from 5% to 50% at a rate of 5%. Notably, the strain sensor could even detect 0.01 mm elongation corresponding to a 0.05% strain, indicating an ultralow detection limit. Moreover, we carry out some additional tests to evaluate the long-term durability and response time of the strain sensors. The strain sensor exhibited good stability and reliability when subjected to over 2000 cycles of repeated loading–unloading with a constant strain of 50% (Fig. 4c). Furthermore, we also compare the sensing behaviors for the sensor after an interval of 1 month or after 15 hours' continuous washing with water while stirring in a beaker, under 10% cyclic stretching–release tests (Fig. 4d). After an interval of 1 month, the resistance of the sensor remains almost unchanged, indicating that the sensor could be used for a long time. Although the resistance of the sensor after washing for 15 hours is slightly increased compared to that of the initial sensor without washing, the sensor still displays good sensing stability and repeatability during the cyclic stretching–release tests. This implies that the TPU@CNT sensor can be washed, which is significant for its application in wearable devices. The response time is another important parameter related to the application of the stretchable strain sensor. In Fig. 4e, it is observed that the TPU@CNT strain sensor exhibits a response time of 75 ms, which is faster than those in most of the previous work.[42–47] In addition, the measured recovery time is 105 ms. The relationship between the relative resistance change ($\Delta R/R_0$) of the sensor and the applied strain is plotted in Fig. 4f. It is worth noting that $\Delta R/R_0$ roughly shows a linear dependence on the applied strain within a strain range from 0.05% to 600%. By linear curve fitting of $\Delta R/R_0$ *versus* strain in Fig. 4f with the strain ranging from 0.05% to 400%, the correlation coefficient of the linear relationship is as high as 0.996. In the strain range from 400% to 600%, the correlation coefficient of the linear relationship is 0.980, indicating the excellent linearity of the sensitivity. Attributed to the good linearity of sensing signals of the TPU@CNT sensor, it can be used to estimate the suffered strain within an ultra-wide strain range from 0.05% to 600%. Recently, there were a few cases that realized an ultrawide strain window by using highly stretchable hydrogels or organogels as the substrates to design the strain sensor.[48–50] For instance, Yin *et al.*[50] reported ionic hydrogel sensors with a broad strain window up to 1400% and a detection limit of 0.5%. However, the resistance exhibited a nonlinear dependence on the applied strain, which limited their practical applications. Up to now, there have not been any reports that have successfully realized an ultra-low detection limit, an ultrawide sensing range and excellent linearity of the sensitivity in one sensor.

In the SEM image of the TPU@CNT strain sensor before stretching (Fig. 5a), it is observed that the surface of the TPU fiber is coated by a layer of CNTs, which are interlocked with each other. Slight stretching can cause slippage of the CNTs, thus resulting in the generation of microcracks on the CNT layer. Although these microcracks are hard to visualize, they can be

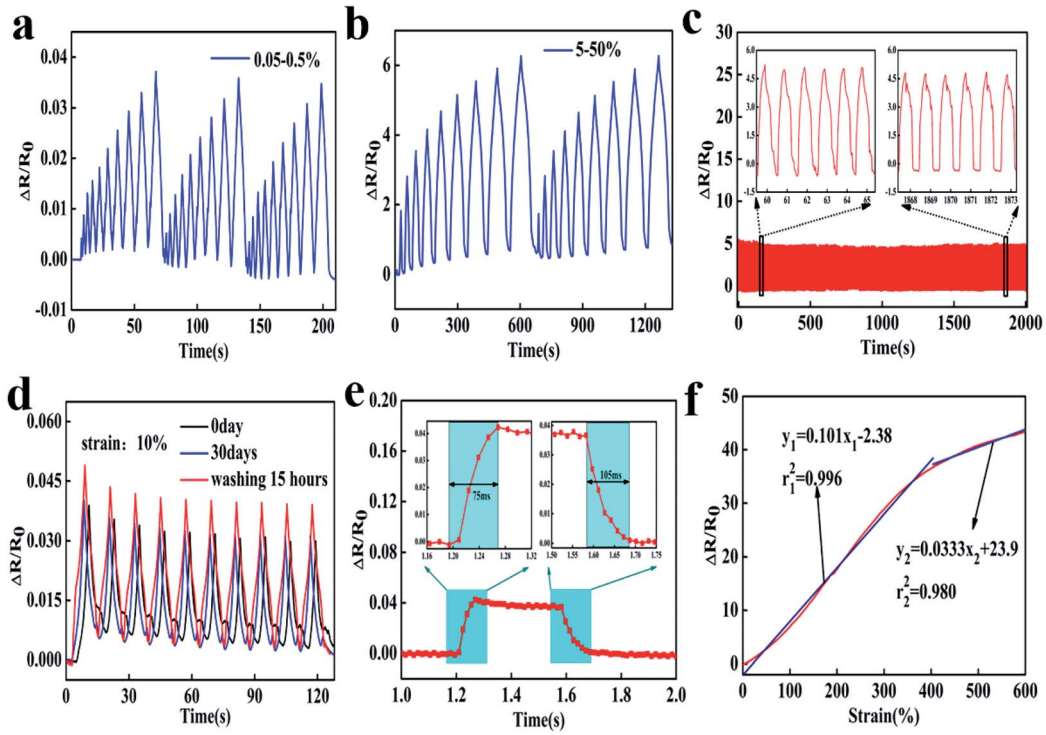

Fig. 4 Dynamic response behaviors of the TPU@CNT sensor during (a) stepwise increase of the strain from 0.05% to 0.5% at a rate of 0.05% or (b) stepwise increase of the strain from 5% to 50% at a rate of 5%; (c) durability test of the TPU@CNT sensor with 2000 stretching–release cycles at a strain of 50%; (d) $\Delta R/R_0$ *vs.* time during the stretching–release cycles at a strain of 10% for the initial TPU@CNT sensor, the sensor after an interval of 30 days, and the sensor after 15 hours' continuous washing with water while stirring in a beaker, respectively; (e) the measurement of the response time and recovery time of the TPU@CNT strain sensor at a strain of 0.05% with a rate of 1000 mm min^{-1}. During the stretching and recovery, there is a 0.3 s pause. (f) The curve of $\Delta R/R_0$ *vs.* strain for the TPU@CNT strain sensor. It shows an excellent linearity within the strain range from 0.05% to 600%.

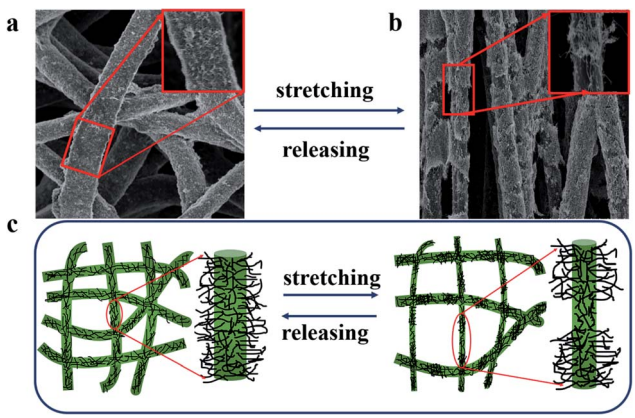

Fig. 5 (a) SEM image of the TPU@CNT strain sensor before stretching; (b) SEM image of the TPU@CNT strain sensor stretched at 100%; (c) the sensing mechanisms of the TPU@CNT strain sensors.

clearly reflected by the electrical signals. In Fig. 3a, it is observed that the sensor resistance is increased *ca.* 0.4% at a strain of 0.05% because of the generation of microcracks on the CNT layer. Under a large strain of 100%, TPU fibers are highly stretched and microcracks develop in the fragmented structures, as shown in Fig. 5b. As a result, the resistance of the TPU@CNT strain sensor is increased significantly. However, attributed to the randomly cross-linked structure of TPU fibers, these conductive pathways between the CNT fragments are still roughly connected. Therefore, the TPU@CNT strain sensor can even suffer and sense the higher strain. To better understand the sensing mechanism of the TPU@CNT strain sensor, a schematic diagram is presented in Fig. 5c. At first, CNTs are highly interlocked with each other to form dense networks on TPU fiber surfaces, which possess lots of contact points between CNTs. Even a very slight deformation of the sensor will cause the slippage of CNTs and then generate microcracks in the CNT layers, endowing the sensor with the ability to sense ultralow strain stimuli. As the sensor is highly stretched, microcracks develop in the fragmented structures because of the long-distance slippage of CNTs, thus causing a continuous increase in electrical resistance. However, the randomly oriented TPU fibers construct the 3D network throughout the stretchable porous sensor. This 3D network ensures that the conductive pathway will not be destroyed completely even at ultrahigh stretching, thus endowing the sensor with an ultrawide sensing range. Attributed to the multi-scale evolution from the microcrack structures to fragmented structures for the conductive network under stretching, the TPU@CNT strain sensor exhibits not only an ultralow detection limit but also an ultrawide sensing range.

Due to a series of superior merits, including good reliability and durability, fast response, an ultralow detection limit and an

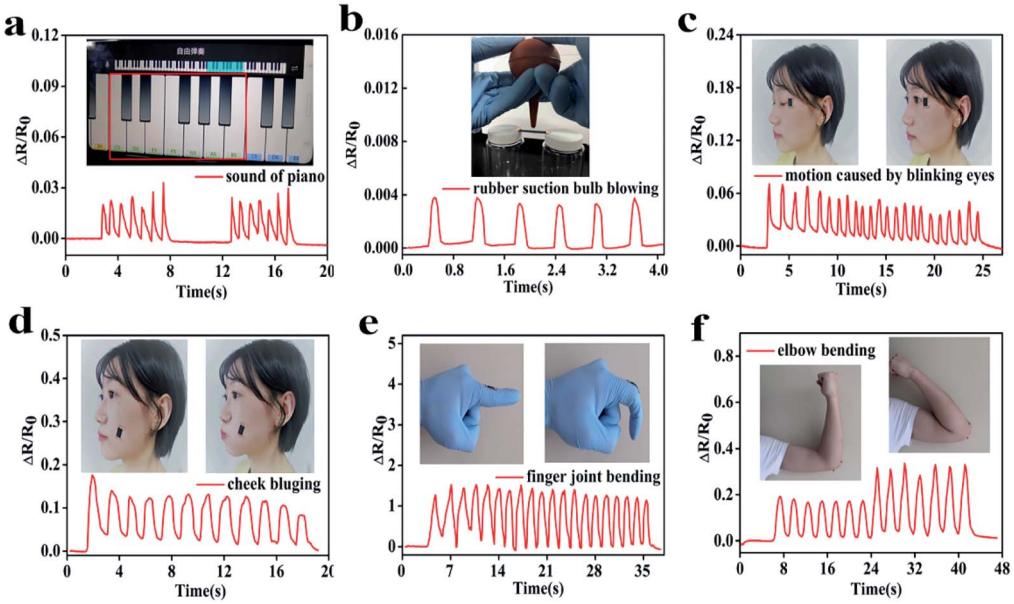

Fig. 6 The demonstration experiments of the TPU@CNT strain sensor in real-time monitoring of human activity and some small physical signals. (a) Detecting the sound of a piano. (b) Detecting the blowing of a rubber suction bulb. (c) Detecting the blinking eyes of a volunteer. (d) Detecting the cheek bulging of a volunteer. (e) Detecting the finger joint bending of a volunteer. (f) Detecting the elbow motion with different bending angles of a volunteer.

ultrawide sensing range, the TPU@CNT strain sensors have great potential in wearable devices and health diagnosis. Some application demonstrations of the TPU@CNT strain sensor are evaluated in Fig. 6. Interestingly, these demonstration experiments indicate that this sensor can detect not only subtle strains such as sound waves but also large strains such as joint motions. From Fig. 6a, it is worth noting that the TPU@CNT strain sensor can even clearly distinguish the notes of "do (1)", "re (2)", "mi (3)", "fa (4)", "sol (5)", "la (6)", and "si (7)" from the density of the resistance. Moreover, the sensor also shows outstanding repeatability since the curve of the second cycle is almost the same as that of the first one. Furthermore, the strain

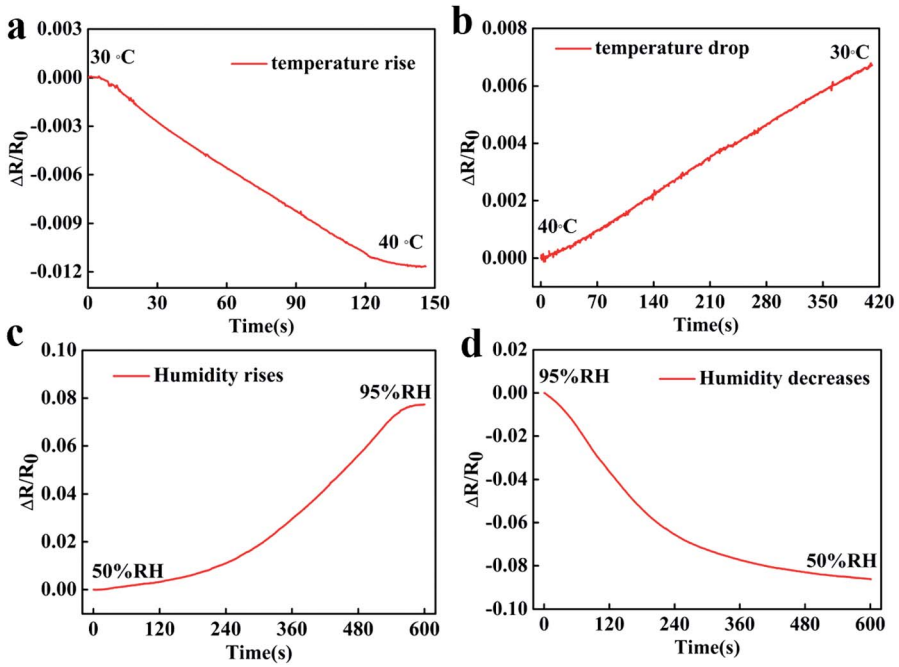

Fig. 7 Resistance response behaviors of the TPU@CNT sensor during (a) stepwise increase of the temperature from 30 °C to 40 °C and (b) stepwise decrease of the temperature from 40 °C to 30 °C, respectively; resistance response behaviors of the TPU@CNT sensor during (c) stepwise increase of the humidity from 50% RH to 95% RH and (d) stepwise decrease of the humidity from 95% RH to 50% RH, respectively.

sensor can also detect the airflow, as shown in Fig. 6b. The sensor is placed between two glass bottles like a bridge and air is blown on it using an ear-washing ball. The sensor vibrates with the blowing, showing a clear cyclic response. If the strain sensor is tightly attached to the surface of human skin using double-sided adhesive, it can be used to detect different-scale motions, as shown in Fig. 6c–f. It can detect the slight motion caused by the blinking of the eyes (Fig. 6c) or the cheek bulging (Fig. 6d). These electrical responses are generated from the movement of the facial muscles, which leads to deformation in the strain sensor attached to the skin. By attaching the sensor to the joints of the human body, real-time physical signal monitoring of finger flexion or elbow motion can be successfully realized (Fig. 6e and f), which can clearly distinguish the states of motion by comparing the shape and intensity of the graphs. For example, different responsivities can be achieved when the tester bends his elbow at different bending angles (Fig. 6f). The response intensity is enhanced with the increase of the bending angle of the elbow because a larger bending angle corresponds to a higher strain, which will cause more damage to the conductive network, thus giving rise to a higher $\Delta R/R_0$. The variations of actual resistance values with time for the above demonstration experiments are presented in the ESI (Fig. S1†).

Since the conductivity of the TPU@CNT sensor highly depends on the interlocked CNT networks on the TPU fiber surface, it may also respond to other stimuli, such as temperature and humidity. It is known that temperature sensors and humidity sensors have great potential in wearable devices and e-skins.[51–55] As shown in Fig. 7a, it is observed that $\Delta R/R_0$ of the TPU@CNT sensor linearly decreases as the temperature is increased from 30 °C to 40 °C. In contrast, $\Delta R/R_0$ linearly increases as temperature is decreased from 40 °C to 30 °C (Fig. 7b). This implies that the TPU@CNT sensor can serve as a temperature sensor, which also exhibits outstanding linear sensitivity to temperature. As the temperature is increased, TPU fibers are softened, thus generating more contact between TPU fibers. As a result, the resistance of the TPU@CNT sensor is decreased. However, the TPU fibers are hardened again with the decrease of temperature, which causes a decrease of contact points between TPU fibers and the increase of the resistance of the sensor. On the other hand, as the environmental humidity of the TPU@CNT sensor is increased, the slight swelling of the TPU fiber may cause minor damage to the conductive network, which results in the increase of resistance of the sensor (Fig. 7c). With the decrease in the environmental humidity, shrinking of the sensor causes the recovery of the conductive network, thus causing a decrease in resistance (Fig. 7d).

4. Conclusion

In this study, a highly stretchable strain sensor is prepared by decorating CNTs on an electrospun TPU fibrous membrane with the assistance of ultrasonication. Attributed to the multi-scale sensing mechanism, the TPU@CNT strain sensor exhibits both an ultralow detection limit and an ultrawide sensing range. Under low strain, the sensing behavior is determined by microcrack structures in the CNT layer. However, fragment structures in the CNT layer determine the sensing properties under large strain. Moreover, the TPU@CNT strain sensor exhibits good durability (showing the same signal even after 15 hours' continuous washing with water under stirring or after an interval of 1 month) and outstanding repeatability (2000 cycles of the stretching–release test). Attributed to these merits, the sensor can not only detect sound waves, but also monitor human motions, displaying promising applications in wearable electronics and soft robotics.

Conflicts of interest

There are no conflicts to declare.

Acknowledgements

This work was financially supported by the National Natural Science Foundation of China for General Program (52073078 and 21774126), the Zhejiang National Science Fund for Distinguished Young Scholars (LR20E030003), and the start-up fund from Hangzhou Normal University.

References

1 M. Nankali, N. M. Nouri, M. Navidbakhsh, N. G. Malek, M. A. Amindehghan, A. M. Shahtoori, M. Karimia and M. Amjadi, *J. Mater. Chem. C*, 2020, **8**, 6185–6195.
2 M. Amjadi, K. U. Kyung, I. Park and M. Sitti, *Adv. Funct. Mater.*, 2016, **26**, 1678–1698.
3 J. Ge, L. Sun, F. R. Zhang, Y. Zhang, L. A. Shi, H. Y. Zhao, H. W. Zhu, H. L. Jiang and S. H. Yu, *Adv. Mater.*, 2015, **28**, 722–728.
4 H. Wang, Z. Liu, J. Ding, X. Lepró, S. Fang, N. Jiang, N. Yuan, R. Wang, Q. Yin, W. Lv, Z. Liu, M. Zhang, R. O. Robles, K. Inoue, S. Yin and R. H. Baughman, *Adv. Mater.*, 2016, **28**, 4998–5007.
5 Y. Zang, F. Zhang, C. Di and D. Zhu, *Mater. Horiz.*, 2015, **2**, 140–156.
6 S. Chen, Z. Lou, D. Chen, K. Jiang and G. Shen, *Adv. Mater. Technol.*, 2016, **1**, 1600136.
7 S. Zhu, J. H. So, R. Mays, S. Desai, W. R. Barnes, B. Pourdeyhimi and M. D. Dickey, *Adv. Funct. Mater.*, 2013, **23**, 2308–2314.
8 S. Zhang, H. Liu, S. Yang, X. Shi, D. Zhang, C. Shan, L. Mi, C. Liu, C. Shen and Z. Guo, *ACS Appl. Mater. Interfaces*, 2019, **11**, 10922–10932.
9 I. You, B. Kim, J. Park, K. Koh, S. Shin, S. Jung and U. Jeong, *Adv. Mater.*, 2016, **28**, 6359–6364.
10 Y. Liu and M. Liu, *Compos. Sci. Technol.*, 2017, **143**, 56–66.
11 S. Zheng, X. Wu, Y. Huang, Z. Xu, W. Yang, Z. Liu, S. Huang, B. Xie and M. Yang, *Composites, Part A*, 2019, **121**, 510–516.
12 H. Wu, Q. Liu, H. Chen, G. Shi and C. Li, *Nanoscale*, 2018, **10**, 17512–17519.
13 N. Lu, C. Lu, S. Yang and J. Rogers, *Adv. Funct. Mater.*, 2012, **22**, 4044–4050.
14 P. Zhan, W. Zhai, N. Wang, X. Wei, G. Zheng, K. Dai, C. Liu and C. Shen, *Mater. Lett.*, 2019, **236**, 60–63.

15 H. Zhu, X. Wang, J. Liang, H. Lv, H. Tong, L. Ma, Y. Hu, G. Zhu, T. Zhang, Z. Tie, Z. Liu, Q. Li, L. Chen, J. Liu and Z. Jin, *Adv. Funct. Mater.*, 2017, **27**, 1606604.
16 K. Suzuki, K. Yataka, Y. Okumiya, S. Sakakibara, K. Sako, H. Mimura and Y. Inoue, *ACS Sens.*, 2016, **1**, 817–825.
17 F. Zhang, S. Wu, S. Peng and C. H. Wang, *Compos. Sci. Technol.*, 2018, **165**, 131–139.
18 S. Wu, J. Zhang, R. B. Ladani, A. R. Ravindran, A. P. Mouritz, A. J. Kinloch and C. H. Wang, *ACS Appl. Mater. Interfaces*, 2017, **9**, 14207–14215.
19 J. Wu, H. Wang, Z. Su, M. Zhang, X. Hu, Y. Wang, Z. Wang, B. Zhong, W. Zhou, J. Liu and S. G. Xing, *ACS Appl. Mater. Interfaces*, 2017, **9**, 38745–38754.
20 T. Q. Trunga and N. E. Lee, *J. Mater. Chem. C*, 2017, **5**, 2202–2222.
21 Y. Qin, Q. Peng, Y. Ding, Z. Lin, C. Wang, Y. Li, F. Xu, J. Li, Y. Yuan, X. He and Y. Li, *ACS Nano*, 2015, **9**, 8933–8941.
22 D. Y. Wang, L. Q. Tao, Y. Liu, T. Y. Zhang, Y. Pang, Q. Wang, S. Jiang, Y. Yang and T. L. Ren, *Nanoscale*, 2016, **8**, 20090–20095.
23 J. Chen, H. Li, Q. Yu, Y. Hu, X. Cui, Y. Zhu and W. Jiang, *Compos. Sci. Technol.*, 2018, **168**, 388–396.
24 J. Chen, Y. Zhu and W. Jiang, *Compos. Sci. Technol.*, 2020, **186**, 107938.
25 J. Chen, Q. Yu, X. Cui, M. Dong, J. Zhang, C. Wang, J. Fan, Y. Zhu and Z. Guo, *J. Mater. Chem. C*, 2019, **7**, 11710–11730.
26 J. Chen, Y. Zhu, J. Huang, J. Zhang, D. Pan, J. Zhou, J. E. Ryu, A. Umar and Z. Guo, *Polym. Rev.*, 2020, DOI: 10.1080/15583724.2020.1734818.
27 L. Li, Y. Zhang, H. Lu, Y. Wang, J. Xu, J. Zhu, C. Zhang and T. Liu, *Nat. Commun.*, 2020, **11**(1), 62.
28 R. Yang, Y. Yao, Z. Duan, Z. Yuan, H. Tai, Y. Jiang, Y. Zheng and D. Wang, *Langmuir*, 2020, **36**, 3029–3037.
29 M. Amjadi, M. Turan, C. P. Clementson and M. Sitti, *ACS Appl. Mater. Interfaces*, 2016, **8**, 5618–5626.
30 X. Liao, Z. Zhang, Q. Liang, Q. Liao and Y. Zhang, *ACS Appl. Mater. Interfaces*, 2017, **9**, 4151–4158.
31 M. Li, H. Li, W. Zhong, Q. Zhao and D. Wang, *ACS Appl. Mater. Interfaces*, 2014, **6**, 1313–1319.
32 D. Kang, P. V. Pikhitsa, Y. W. Choi, C. Lee, S. S. Shin, L. Piao, B. Park, K. Y. Suh, T. Kim and M. Choi, *Nature*, 2014, **516**(7530), 222–226.
33 A. Singh, H. Watanabe, H. Watanabe and H. Lee, *ACS Appl. Electron. Mater.*, 2020, **2**, 523–528.
34 X. Liao, Z. Zhang, Z. Kang, F. Gao, Q. Liao and Y. Zhang, *Mater. Horiz.*, 2017, **4**, 502–510.
35 C. Wang, K. Xia, M. Jian, H. Wang, M. Zhang and Y. Zhang, *J. Mater. Chem. C*, 2017, **5**, 7604–7611.
36 M. Ren, Y. Zhou, Y. Wang, G. Zheng, K. Dai, C. Liu and C. Shen, *Chem. Eng. J.*, 2019, **360**, 762–777.
37 J. Lee, S. Pyo, D. S. Kwon, E. Jo, W. Kim and J. Kim, *Small*, 2019, **15**, 1805120.
38 Z. Sun, S. Yang, P. Zhao, J. Zhang, Y. Yang, X. Ye, X. Zhao, N. Cui, Y. Tong, Y. Liu, X. Chen and Q. Tang, *ACS Appl. Mater. Interfaces*, 2020, **12**, 13287–13295.
39 Q. Li, H. Liu, S. Zhang, D. Zhang, X. Liu, Y. He, L. Mi, J. Zhang, C. Liu, C. Shen and Z. Guo, *ACS Appl. Mater. Interfaces*, 2019, **11**, 21904–21914.
40 J. Lin, X. Cai, Z. Liu, N. Liu, M. Xie, B. Zhou, H. Wang and Z. Guo, *Adv. Funct. Mater.*, 2020, **30**, 2000398.
41 Z. He, G. Zhou, J. H. Byun, S. K. Lee, M. K. Um, B. Park, T. Kim, S. Lee and T. W. Chou, *Nanoscale*, 2019, **11**, 5884–5890.
42 C. Z. Hang, X. F. Zhao, S. Y. Xi, Y. H. Shang, K. P. Yuan, F. Yang, Q. G. Wang, J. C. Wang, D. W. Zhang and H. L. Lu, *Nano Energy*, 2020, **76**, 105064.
43 Z. Tang, S. Jia, F. Wang, C. Bian, Y. Chen, Y. Wang and B. Li, *ACS Appl. Mater. Interfaces*, 2018, **10**, 6624–6635.
44 C. G. Zhou, W. J. Sun, L. C. Jia, L. Xu, K. Dai, D. X. Yan and Z. M. Li, *ACS Appl. Mater. Interfaces*, 2019, **11**, 37094–37102.
45 Y. Wang, M. Tebyetekerwa, Y. Liu, M. Wang, J. Zhu, J. Xu, C. Zhang and T. Liu, *Chem. Eng. J.*, DOI: 10.1016/j.cej.2020.127637.
46 Z. Duan, Y. Jiang, S. Wang, Z. Yuan, Q. Zhao, G. Xie, X. Du and H. Tai, *ACS Sustainable Chem. Eng.*, 2019, **7**, 17474–17481.
47 T. Sun, D. Jiang, Z. Duan, Z. Yuan, Y. Wang and H. Tai, *Sci. China: Technol. Sci.*, 2020, DOI: 10.1007/s11431-019-1567-y.
48 M. Wu, J. Chen, Y. Ma, B. Yan, M. Pan, Q. Peng, W. Wang, L. Han, J. Liu and H. Zeng, *J. Mater. Chem. A*, 2020, **8**, 24718–24733.
49 X. Guo, C. Zhang, L. Shi, Q. Zhang and H. Zhu, *J. Mater. Chem. A*, 2020, **8**, 20346–20353.
50 J. Yin, S. Pan, L. Wu, L. Tan, D. Chen, S. Huang, Y. Zhang and P. He, *J. Mater. Chem. C*, 2020, DOI: 10.1039/d0tc04144k.
51 N. Forintosa and T. Cziganya, *Composites, Part A*, 2020, **131**, 105819.
52 H. Tai, Z. Duan, Y. Wang, S. Wang and Y. Jiang, *ACS Appl. Mater. Interfaces*, 2020, **12**, 31037–31053.
53 Z. Duan, Y. Jiang, M. Yan, S. Wang, Z. Yuan, Q. Zhao, P. Sun, G. Xie, X. Du and H. Tai, *ACS Appl. Mater. Interfaces*, 2019, **11**, 21840–21849.
54 Y. Wang, S. Hou, T. Li, S. Jin, Y. Shao, H. Yang, D. Wu, S. Dai, Y. Lu, S. Chen and J. Huang, *ACS Appl. Mater. Interfaces*, 2020, **12**, 41896–41904.
55 W. Ye, Q. Cao, X. Cheng, C. Yu, J. He and J. Lu, *J. Mater. Chem. A*, 2020, **8**, 17675–17682.

